

# In-situ nano-precipitation enables superior cryogenic mechanical properties in a 3D printable medium-entropy alloy

Received: 29 July 2025

Accepted: 26 November 2025

Published online: 12 December 2025

 Check for updates

Tiwen Lu<sup>1,7</sup>, Xiyu Chen<sup>1,7</sup>, Binhan Sun<sup>1</sup>  , Xizhen Dong<sup>2</sup>, Ning Yao<sup>1</sup>, Yufei Chen<sup>1</sup>, Zhongji Sun<sup>3</sup>, Hongyu Chen<sup>4</sup>, Alisson Kwiatkowski da Silva<sup>2</sup>, Haitao Lu<sup>1</sup>, Xiaofeng Yang<sup>1</sup>, Bingbing Wan<sup>5</sup>, Jianping Tan<sup>1</sup>, Sergio Scudino<sup>6</sup>, Xian-Cheng Zhang<sup>1</sup>  , Dierk Raabe<sup>2</sup>   & Shan-Tung Tu<sup>1</sup> 

Precipitates or second-phase particles effectively strengthen metallic materials. Their use in additive manufacturing (AM), however, is constrained by the narrow thermal window of laser processing, which restricts control over precipitate characteristics. Here, we overcome this problem by creating a novel cryogenically strong and ductile alloy by a size-dependent composite powder feedstock design consisting of CoCrNi medium-entropy alloy core powders and decorated TiC shell nanoparticles. We show that these compound particles can be completely dissolved into the alloy during the first laser pulse of AM and then reprecipitate in situ upon subsequent cyclic reheating. Consequently, we introduce a high number density of nanosized TiC precipitates, coherent with the matrix. Their strong resistance to dislocation glide increases tensile strength by ~312 MPa and promotes dislocation accumulation without inducing severe stress heterogeneity or premature cracking, yielding a high strength-ductility product at 87 K. Our in-situ nano-precipitation strategy is achieved by laser-induced melting of pre-assembled nanoparticles and their kinetically favorable reprecipitation, which is applicable to other AM alloy systems to enhance their cryogenic mechanical properties.

Metal-based additive manufacturing, or three-dimensional (3D) printing, is recognized as a disruptive metal processing technology with numerous unique advantages. One notable benefit is the capability to fabricate complex component geometries with minimum material waste, offering a sustainable solution particularly for certain industry sectors (e.g., aerospace and energy) that require to use massive resource-intensive metallic materials<sup>1,2</sup>. In comparison to their cast and thermo-mechanically processed counterparts, additively

manufactured (AM) materials often possess a higher strength<sup>3-6</sup>, due to the rapid cooling-induced high dislocation density<sup>3-5</sup> and grain substructures<sup>6</sup>. However, the increased strength, along with unavoidable manufacturing defects and chemical segregations in AM materials, impairs their ductility and damage-tolerance especially at harsh environments like cryogenic temperatures<sup>7-9</sup>. For instance, the recently developed face-centered cubic (FCC) CoCrNi medium-entropy alloy (MEA), one of the toughest alloys in its cast and

<sup>1</sup>Key Laboratory of Pressure Systems and Safety, Ministry of Education, East China University of Science and Technology, Shanghai, China. <sup>2</sup>Max Planck Institute for Sustainable Materials, Düsseldorf, Germany. <sup>3</sup>Institute of Materials Research and Engineering, Agency for Science, Technology and Research (A\*STAR), Singapore, Singapore. <sup>4</sup>Key Laboratory of Impact and Safety Engineering, Ministry of Education, Ningbo University, Ningbo, China. <sup>5</sup>School of Materials Science and Engineering, Dongguan University of Technology, Dongguan, China. <sup>6</sup>Leibniz Institute for Solid State and Materials Research Dresden, Dresden, Germany. <sup>7</sup>These authors contributed equally: Tiwen Lu, Xiyu Chen. ✉ e-mail: [binhan.sun@ecust.edu.cn](mailto:binhan.sun@ecust.edu.cn); [xczhang@ecust.edu.cn](mailto:xczhang@ecust.edu.cn); [d.raabe@mpie.de](mailto:d.raabe@mpie.de)

thermo-mechanically treated state at cryogenic temperatures<sup>10,11</sup>, was reported to experience premature failure at the temperature range of 77–143 K when the alloy is produced by additive manufacturing<sup>7,8</sup>. This shortcoming of AM materials strongly limits their deployment in safety-critical cryogenic infrastructures that are needed for sustainable energy supply and transportation.

In comparison to conventional manufacturing routes that can afford the flexibility of multi-step thermomechanical processing to fine-tune alloys' microstructures for enhanced strength-ductility synergy, AM parts have less freedom of post-processing (such as heat treatment), due to the potential risk for the degradation of their dimensional accuracy<sup>12,13</sup> and the formation of heat-induced cracks<sup>14</sup>. In-situ microstructure tuning, which exploits phase transformations during the process of additive manufacturing is thus desired<sup>15,16</sup>. However, the often unmanageable temperature profile and narrow time window inherent in laser additive manufacturing pose significant challenges in controlling microstructure characteristics (e.g., phase fraction, size, distribution, and interface coherence)<sup>11,17</sup>. This is particularly true for AM materials that utilize pre-assembled metallic or ceramic particles to introduce second phases within the microstructure for strengthening<sup>18–20</sup>. The strengthening, resulting from the blocking effect of second phases on dislocation motion, typically increases with the strength and stiffness of the second phase used<sup>21</sup>. However, strong and stiff particles generally possess much higher melting points than the matrix materials in which they are embedded due to their strong covalent or ionic bonds<sup>22,23</sup>. This means that high-strength second-phase particles are difficult to be dissolved in matrix during laser melting, which further impedes their metallurgical control. Instead, they often form unpredictably distributed incoherent particles already during solidification<sup>24</sup>, which readily results in damage nucleation upon mechanical loading and thus a risk of embrittlement at cryogenic temperatures<sup>25,26</sup>. Fundamental challenges thus arise pertaining to how to utilize and control high-strength

particles in AM materials to improve both strength and ductility at cryogenic temperatures.

Here, we provide an additive manufacturing solution to reconcile the above-mentioned conflict, namely, (i) bringing finely dispersed stiff particles with high melting points into a metallic alloy and (ii) devising a process that allows for their full metallurgical and process control. We find that through a size-dependent composite powder feedstock design (Fig. 1a), hard TiC nanoparticles (melting temperature ~3413 K<sup>27</sup>) coated on CoCrNi MEA powder particles (which serve in their uncoated state as the base matrix alloy) can be completely dissolved in the alloy during the first laser energy pulse. The subsequent laser pulses and the associated cyclic reheating enable their preferential reprecipitation in a highly dispersed, nanosized, and coherent manner. The high resistance to dislocation motion caused by these precipitates gives rise to a high tensile strength at the cryogenic temperature as well as a highly intensive dislocation interaction and accumulation that is crucial for strain hardening. We further observe that these coherent nanoprecipitates also effectively suppress the low-temperature induced intergranular cracking observed in the reference AM CoCrNi alloy devoid of such nanoprecipitates, due to the mitigated grain boundary-dislocation interactions and the resulting more homogenous stress and strain patterns. The key for such cryogenic mechanical performance lies in the size-dependent composite feedstock induced nano-precipitation, a process that is controllable and applicable for other FCC alloys. Our work hence widens the processing toolbox that so far lacked effective means for additively manufactured alloys to withstand harsh cryogenic environments.

## Results and Discussion

### Microstructural characteristics

The equiatomic CoCrNi metal powders (diameter 15–53  $\mu\text{m}$ ) coated with nanosized (average diameter ~190 nm, Supplementary Fig. 2) TiC particles (Fig. 1b) have good printability that enables successful

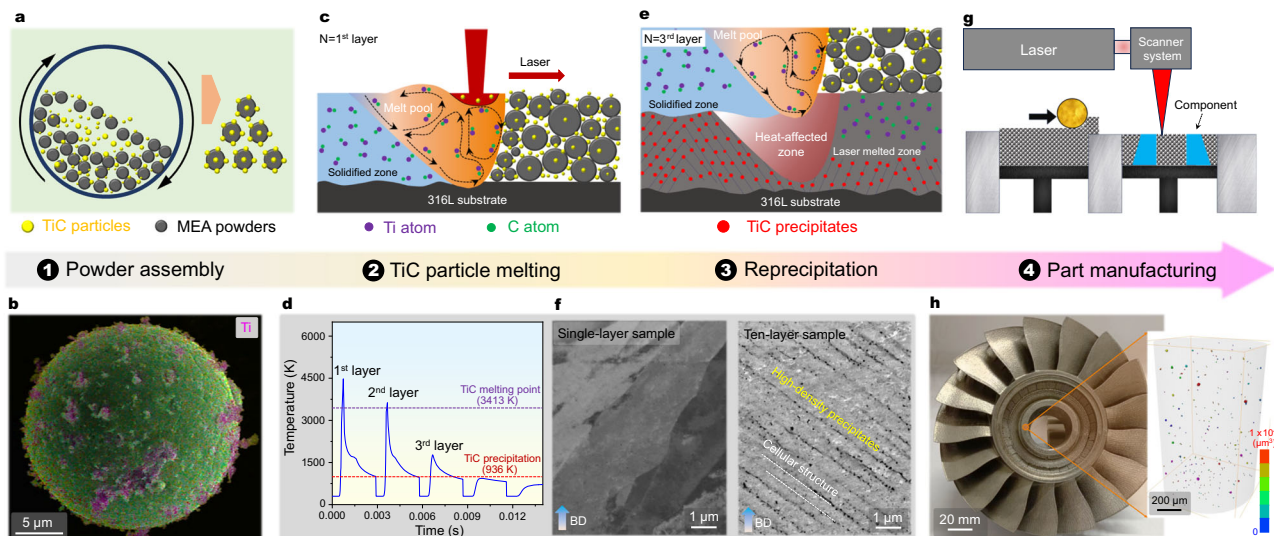


**Fig. 1 | Additive manufacturing process utilizing size-controlled TiC-CoCrNi composite powders.** **a** Schematic diagram showing the process of powder assembly using CoCrNi and TiC powders. **b** A typical secondary electron (SE) image overlaid with energy-dispersive X-ray spectroscopy (EDX) Ti mapping, showing the morphology of powder mixture consisting of CoCrNi powders and coated TiC nanoparticles. **c, e** Schematics of TiC melting and reprecipitation. **d** The simulated temperature-time profile of a specific location within the first layer during a single-track multi-layer additive manufacturing process. The melting temperature of TiC (~3413 K<sup>27</sup>) and its reprecipitation temperature from solid solution (936 K, calculated from the Thermo-Calc software with the TCHEA4 database) are also marked. **f** The electron channeling contrast imaging (ECCI) of the single-layer and ten-layer nTiC-CoCrNi samples made by single-track laser powder bed fusion (L-PBF) process,

revealing the complete dissolution of pre-assembled TiC nanoparticles during the first laser pulse and their reprecipitation during the subsequent laser pulses and the associated cyclic reheating. These single-layer and ten-layer samples were single-track thin walls using the same L-PBF processing parameters as the bulk sample. **g, h** Additive manufacturing of a turbine blade using TiC nanoparticle-decorated CoCrNi composite powders, showing a good printability. The inset in (h) is the micro-computed tomography ( $\mu$ -CT) results of a cylinder taken from the blade, showing the spatial and size distributions of printing defects. The scanning strategy and sample size is shown in Supplementary Fig. 1. These schematic diagrams were created by PowerPoint software. Source data are provided as a Source Data file.

fabrication of components with complex geometries (see the printed turbine blade as an example, Fig. 1h). The sample consolidated by laser powder bed fusion (L-PBF) shows a high density of >99.8%, with only few manufacturing defects (small gas pores) as shown by the micro-computed tomography ( $\mu$ -CT) results (the inset in Fig. 1h). The microstructure of the as-printed nano-TiC-decorated CoCrNi alloy (referred to as nTiC-CoCrNi) has an FCC matrix, with a tortuous grain morphology (average grain size  $\sim$ 22.7  $\mu$ m, Fig. 2a). Scanning transmission electron microscopy (STEM) analysis in Fig. 2b reveals the presence of solidification cellular substructures within each grain. The average diameter of the cellular structure is  $529 \pm 116$  nm. Along the cellular boundaries, pronounced Cr and Ti segregation is observed in Fig. 2c. The concentration of Cr and Ti at cellular and grain boundaries was measured to be  $\sim$ 36 at.% and 3.3 at.%, respectively, which is around  $\sim$ 3 at.% and  $\sim$ 1.5 at.% higher than its concentration value within grain interior (Supplementary Fig. 3). Such segregation derives from solute partitioning between liquid and solid phases in the interdendritic regions during solidification<sup>28</sup>.

The above-mentioned microstructure features of the nTiC-CoCrNi sample (matrix phase, grain size, cellular substructure and solute segregation) are similar to those in the reference AM CoCrNi sample that has been fabricated using pure CoCrNi powders alone, i.e. without any nanoparticle coated powders (microstructure shown in Supplementary Fig. 4). The main difference is the presence of a high number density ( $\sim 4.9 \times 10^{20} \text{ m}^{-3}$ ) of Ti-rich nanoprecipitates (average diameter of  $\sim$ 36 nm), which are found to form at cellular boundaries in the nTiC-CoCrNi sample, as indicated from the energy-dispersive X-ray spectroscopy (EDX) results in Fig. 2c. High-resolution transmission electron microscopy (HR-TEM) and fast Fourier transform (FFT) analysis reveal an FCC structure of the nanoprecipitates (Fig. 2d), with their room-temperature lattice parameter (0.43 nm) matching well to that of TiC (0.43 nm<sup>29</sup>). The interplane spacing of their (200) planes (0.215 nm) is very close to that of parallel (111) planes of the FCC matrix (0.217 nm, Fig. 2e and Supplementary Fig. 5), suggesting a low lattice mismatch (0.75%) and thus a coherent nature between the nanoprecipitates and matrix.

Different from using nano-particles on powder feedstock to influence solidification behavior, the starting point of our work is to introduce better precipitation strengthening effect to fabricate AM materials with superior cryogenic mechanical properties. To study the underlying formation mechanisms of these TiC nanoprecipitates, we characterize the microstructure of single-layer and ten-layer nTiC-CoCrNi samples after a single-track L-PBF process. We find that the pre-assembled nanosized TiC particles had been completely dissolved after first-layer laser melting (Fig. 1f), whereas TiC reprecipitation occurs during the further L-PBF process (Fig. 1f). The temperature history simulation for a specific location in the first layer reveals that the intrinsic cyclic heating induced by laser melting at the third layer is higher than the TiC precipitation temperature (936 K, as calculated by thermodynamic simulations, Supplementary Fig. 6). Ti segregation at the cellular boundaries promotes the formation of Ti-rich precipitates. The absence of large-sized remaining TiC particles present in the matrix confirms that reprecipitation behavior should be occurred in the solid state induced by intrinsic cyclic heating. Another item to proof TiC reprecipitation comes from atom probe tomography (APT) results (Fig. 2f), which show the presence of not only Ti and C, but also substantial Cr and Ni (up to 20 at.% for each element) within the nanoprecipitate. The latter two elements are not expected to heavily concentrate in TiC precipitates in equilibrium (Supplementary Fig. 6). We attribute this phenomenon to the insufficient element partitioning between the matrix and TiC precipitates as a response to the fast cyclic heating cycles at temperatures above  $\sim$ 936 K (Fig. 1d).

It should be noted that due to the high melting point of TiC particles ( $\sim$ 3413 K<sup>27</sup>), their initial size before L-PBF needs to be carefully controlled to ensure a complete dissolution during the short

manufacturing process. To demonstrate this point, we also compare the microstructure between our nTiC-CoCrNi sample and another AM CoCrNi-based alloy that is fabricated based on CoCrNi powders mixed with larger (micron-sized) TiC particles (average diameter  $\sim$ 10  $\mu$ m, Supplementary Fig. 7). For the latter sample (referred to as  $\mu$ TiC-CoCrNi), we observe that the pre-assembled TiC particles are indeed not completely dissolved upon rapid laser melting and cooling due to the large particle size. The DICTRA simulation discovers that the size threshold for the complete dissolution of TiC particles during the first laser pulse is  $\sim$ 3.2  $\mu$ m (Fig. 2h). Instead, the undissolved TiC remains distinctly incoherent to the matrix (Fig. 2i), thus lacking lattice compliance, which might promote damage initiation. The characteristics of TiC play a pivotal role in the mechanical performance of the investigated alloys at cryogenic temperatures, which will be discussed as follows.

### Mechanical properties

The in-situ formation of a high number density of coherent TiC nanoprecipitates results in an exceptional strength (yield strength  $\sim$ 1.2 GPa, ultimate tensile strength  $\sim$ 1.7 GPa) and ductility (fracture strain  $\sim$ 36.7 $\pm$ 1.6%) of our new nTiC-CoCrNi alloy at the cryogenic temperature (87 K), as displayed in Fig. 3a. Figure 3b shows that at the same yield strength level, the product of tensile strength and ductility of our alloy has surpassed that of all other AM metallic materials (by at least 54%) that have been reported to date. A combination of high strength and high ductility means that the material has great energy dissipation capability without fracturing<sup>30</sup>. To elucidate the governing mechanisms behind the beneficial effects of the coherent TiC nanoprecipitates in this size-controlled powder assembly process, we compare the nTiC-CoCrNi alloy with two reference materials, namely, the AM CoCrNi alloy devoid of any precipitates and the  $\mu$ TiC-CoCrNi sample containing unmelted incoherent micron-sized TiC particles. We observe that the presence of TiC particles, regardless of their size and coherence, results in an improvement of yield strength at the cryogenic temperature, more specifically, by  $\sim$ 225 MPa for the nTiC-CoCrNi sample and  $\sim$ 270 MPa for the  $\mu$ TiC-CoCrNi sample (detailed strengthening mechanisms shown in Supplementary Note 2). The most intriguing phenomenon is that the ductility of our nTiC-CoCrNi sample is simultaneously enhanced by 30.1% in comparison to the reference AM CoCrNi sample (Fig. 3a). This enhancement of inelastic formability is attributed to its higher and more persistent strain-hardening capability that shifts strain localization (i.e., necking, Fig. 3d) to larger total deformations and to the suppression of damage initiation that is often induced by incoherent coarse second phases. The latter feature in the nTiC-CoCrNi sample is in sharp contrast to both the AM CoCrNi and the  $\mu$ TiC-CoCrNi samples which experience premature failure at the test temperature due to low-temperature induced early damage formation and thus a certain degree of ductility loss (Fig. 3c). The absence of ductility loss along with the exceptional strength-ductility combination achieved in the nTiC-CoCrNi sample also ensures a markedly high fracture toughness ( $K_{JIC} = 267.3 \pm 5.3 \text{ MPa}\cdot\text{m}^{0.5}$ , Supplementary Fig. 9), significantly outperforming that of the AM CoCrNi ( $K_{JIC} = 169.3 \pm 9.0 \text{ MPa}\cdot\text{m}^{0.5}$ ) and  $\mu$ TiC-CoCrNi ( $K_{JIC} = 123.9 \pm 10.5 \text{ MPa}\cdot\text{m}^{0.5}$ ) samples at the same cryogenic temperature (87 K) and with the same orientation (i.e., the notch plane of the compact-tension (C(T)) specimens and the crack propagation direction were both perpendicular to the building direction). These comparisons thus underscore the efficacy of our microstructural strategy in reconciling strength, ductility and toughness, a formidable challenge within the realm of metal additive manufacturing, specifically tailored for cryogenic applications.

### Deformation behavior

We next unravel the underlying strengthening and ductilization mechanisms associated with the coherent TiC nanoprecipitates. For this purpose, we deform the sample at different strain levels and probe

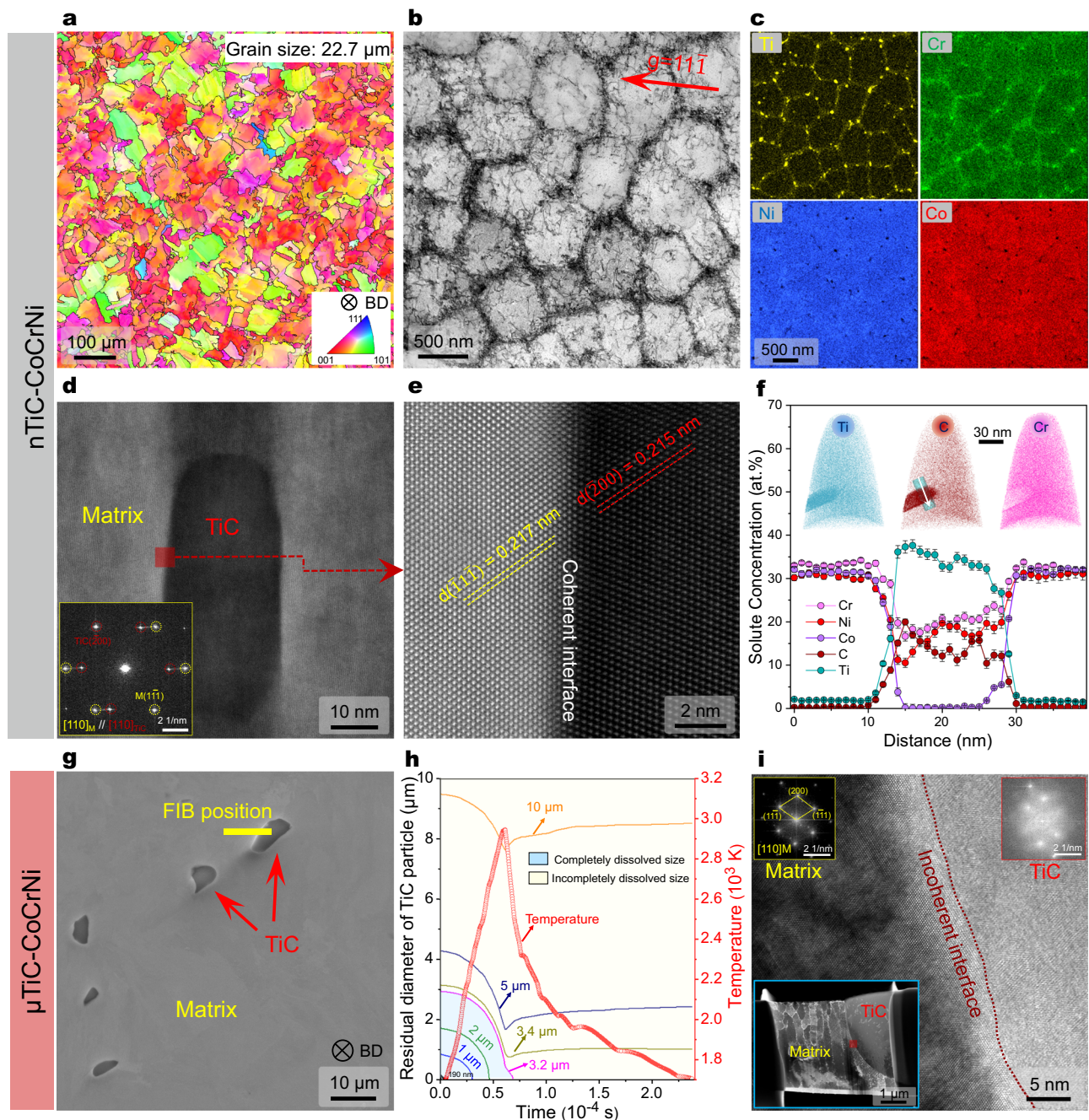


**Fig. 2 | The as-printed microstructure of the nTiC-CoCrNi and  $\mu$ TiC-CoCrNi samples.** **a** Electron backscatter diffraction (EBSD) inverse pole figure (IPF) perpendicular to the building direction, showing the grain morphology and size of the nTiC-CoCrNi sample. **b** Bright-field (BF) scanning transmission electron microscopy (STEM) image taken within one grain under the  $g=11\bar{1}$  diffraction vector, showing cellular structures with an average size of  $-529\pm 116$  nm. **c** TEM-EDX maps of Co, Cr, Ni, and Ti, taken from the same area as **b**, showing the segregation of Cr and the formation of Ti-rich nanoprecipitates along with the cellular boundaries. **d** High-resolution transmission electron microscopy (HR-TEM) image of a nanoprecipitate embedded in the matrix and fast Fourier transform (FFT) pattern taken from the  $[110]$  zone axis, showing the orientation relationship of  $(200)\text{TiC} // (\bar{1}\bar{1}\bar{1})$  matrix and  $[110]\text{TiC} // [110]$  matrix. **e** Magnified interface region taken from the rectangular frame in **(d)**, showing the coherent nature of the TiC-matrix interface.

The measurement results of the interplane spacing of the TiC nanoprecipitate and the matrix are displayed in Supplementary Fig. 5. **f** Atom probe tomography (APT) concentration profile across the precipitate. The reconstructed atomic maps of Ti, C, and Cr are also inset, indicating the position of the nanoprecipitate. **g** SE image of the  $\mu$ TiC-CoCrNi sample, showing the presence of undissolved TiC particles. **h** The simulated residual particle diameter after the single-track L-PBF process using different TiC particle size. Detailed simulation methods are shown in Supplementary Fig. 8. **i** HR-TEM image showing the incoherent nature between undissolved TiC and the FCC matrix. The insert is a TEM overview image taken from the focused ion beam (FIB) slice marked in **(g)**, containing the matrix and a micron-sized TiC particle. The error bars represent standard deviation. Source data are provided as a Source Data file.

the substructures by electron backscatter diffraction (EBSD) and TEM. Typically, in other FCC materials (e.g. other multicomponent alloys<sup>31,32</sup>, Fe-based alloys<sup>33,34</sup>, and Ni-based superalloys<sup>35</sup>), coherent precipitates (e.g.,  $L1_2$ -typed carbides) with similar size ( $\sim 50$  nm) are often sheared

by dislocations (Supplementary Table 2). However, here in our nTiC-CoCrNi sample, we observe that dislocations bypass TiC nanoprecipitates and form dislocation loops, as demonstrated in the 4% strained sample in Fig. 4a-d and Supplementary Fig. 11, suggesting the

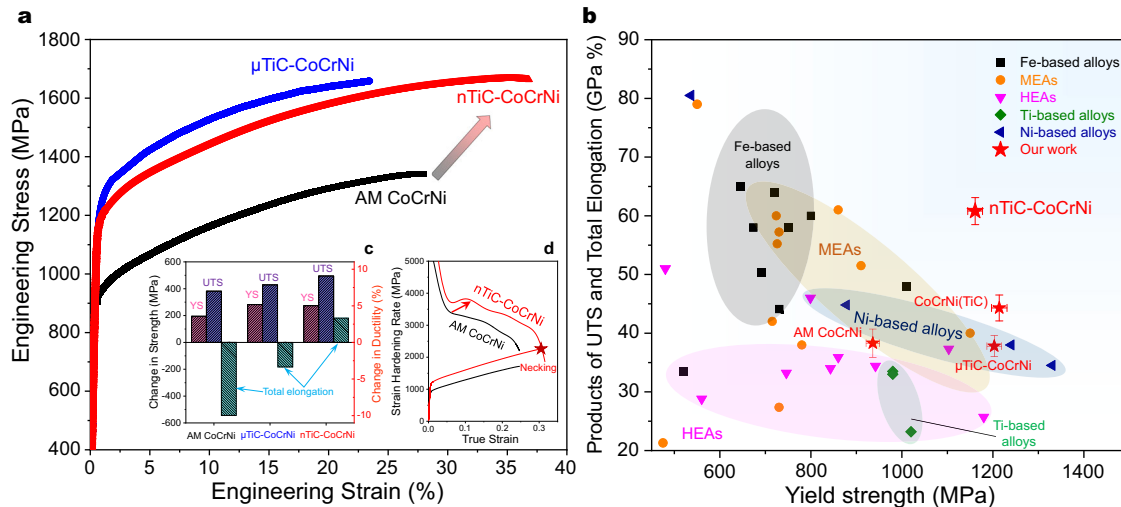


**Fig. 3 | Cryogenic tensile property of the additively manufactured alloys at 87 K.** **a** Engineering stress-strain curves of our nTiC-CoCrNi sample containing coherent TiC nanoprecipitates, in comparison to the reference AM CoCrNi sample and the  $\mu$ TiC-CoCrNi sample with micron-sized incoherent TiC precipitates. The long axes of the tensile specimens are perpendicular to the building direction, and the tensile properties of other orientations and fracture toughness are shown in Supplementary Fig. 9 and 10. The inset **c** displays the change in yield strength, ultimate tensile strength, and total elongation of the three samples when the temperature decreases from 298 K to 87 K. nTiC-CoCrNi sample displays a simultaneous improvement in strength and ductility at the cryogenic temperature,

whereas the AM CoCrNi and  $\mu$ TiC-CoCrNi samples show a decreased ductility. The inset **d** shows the strain-hardening-rate curves of the AM CoCrNi and nTiC-CoCrNi samples at 87 K. **b** The product of cryogenic tensile strength and total elongation as a function of yield strength of the studied materials with the same orientation, in comparison to other AM alloys tested at near liquid-nitrogen temperature (77–87 K), including various medium/high entropy alloys<sup>8,9,55–60</sup>, Fe-based alloys<sup>61–64</sup>, Ni-based alloys<sup>65,66</sup>, and Ti-based alloy<sup>67</sup>. More details of the literature data are listed in Supplementary Table 1. The error bars represent standard deviation. Source data are provided as a Source Data file.

prevalence of the Orowan mechanism rather than dislocation shearing. This phenomenon results from the large mismatch in the shear modulus between the stiff nanoprecipitate (182 GPa<sup>36</sup>) and the matrix (93 GPa<sup>11</sup>), which gives rise to a markedly high particle shearing stress (estimated to be as high as 1.3 GPa, Supplementary Note 1). Therefore, dislocations are completely blocked by the high number density of non-shearable TiC precipitates, which contributes to a significant strengthening effect (calculated to be 256 MPa on the basis of the Orowan strengthening mechanism, Supplementary Note 2). Further, the blocking, trapping and the resulting patterning of dislocations by the precipitates and the surrounding Orowan dislocation loops with the same sign promote the gradually evolving storage and formation of new dislocations. This is a critical precondition for the high strain hardening observed in the nTiC-CoCrNi sample (Fig. 3d). The new dislocations can either be nucleated from original dislocation sources (e.g. Frank-Read sources and grain boundaries) or directly emitted from the TiC-matrix interfaces due to the high stress concentrations therein (as exhibited in Fig. 4d). As a result, an increased dislocation multiplication rate (by a factor of ~1.6 in comparison to the TiC-free AM CoCrNi counterpart material, as shown from Fig. 4i) and the resulting stronger dislocation interactions are achieved in the nTiC-CoCrNi material. We believe that this is the major reason for the observed rise in the strain hardening rate found for this alloy at a strain of ~4% (marked by an arrow in Fig. 3d). At a higher strain level of ~18% (Fig. 4e-h) and beyond (Fig. 4i-k), deformation nano-twins start to form in the nTiC-CoCrNi alloy, subdividing its cellular substructure (Fig. 4f and g) and limiting the average dislocation mean free path (Fig. 4j) through the progressive introduction of new interfaces. The rapid dislocation generation leveraged by the TiC nanoprecipitates, along with the effects of deformation twinning on dislocation multiplication and motion, accelerate both statistically stored dislocations and geometrically necessary dislocations (GNDs) during deformation of this material (Fig. 4k and l). In particular, we find that in the nTiC-CoCrNi sample the back-stress hardening, induced by dislocation pile-ups at grain and twin boundaries as well as by GNDs formed due to elastic and

plastic incompatibility between TiC and the matrix, is much higher than that of the AM CoCrNi reference sample (Supplementary Fig. 12). Therefore, it can be concluded that the presence of non-shearable TiC precipitates and their interactions with dislocations contribute to both isotropic and kinematic hardening, which jointly increase the strain-hardening ability of the material. It is worthwhile to note that in the latter material, a high interface density of deformation twins (DTs) is also formed, even at a smaller strain of ~4% (Supplementary Fig. 13). This finding strongly suggests that the high and permanently maintained strain hardening rate observed in the nTiC-CoCrNi sample is closely linked to the presence of TiC nanoprecipitates and their non-shearable nature and less to the twins.

### Fracture mechanism

Unlike traditionally cast and thermomechanically treated FCC materials, the reference AM CoCrNi sample suffers from a certain degree of ductility loss at the testing temperature of 87 K, which causes premature failure as shown in Fig. 3d. Characterization of the fracture surface of this sample, from both, a side view (EBSD data in Fig. 5a and b) and front view (SEM fractography in Fig. 5c), reveals that such failure mainly stems from the intergranular cracking along grain boundaries (GBs). We ascribe this low-temperature induced cracking event to the following two factors. Firstly, the segregation of Cr at GBs reduces the cohesive energy of GBs, i.e., the interface is weakened<sup>37,38</sup>. This is due to the increased GB energy (Supplementary Fig. 14) induced by the atomic size difference as well as the changes in the local electronic structure<sup>39</sup>. Secondly, the blocking effect of GBs on dislocations and deformation twins results in a high stress concentration at the GBs<sup>40</sup>. The latter point is supported by a more detailed observation of the microstructure near the fracture surface (Fig. 5d), which shows indeed the formation of microcracks at the twin-GB intersections.

In contrast to the AM CoCrNi sample, we find that the grain boundary cracking and intergranular fracture are completely suppressed in the nTiC-CoCrNi material (Fig. 5e-g), even in regions very close to the fracture surface (which experience the highest level of

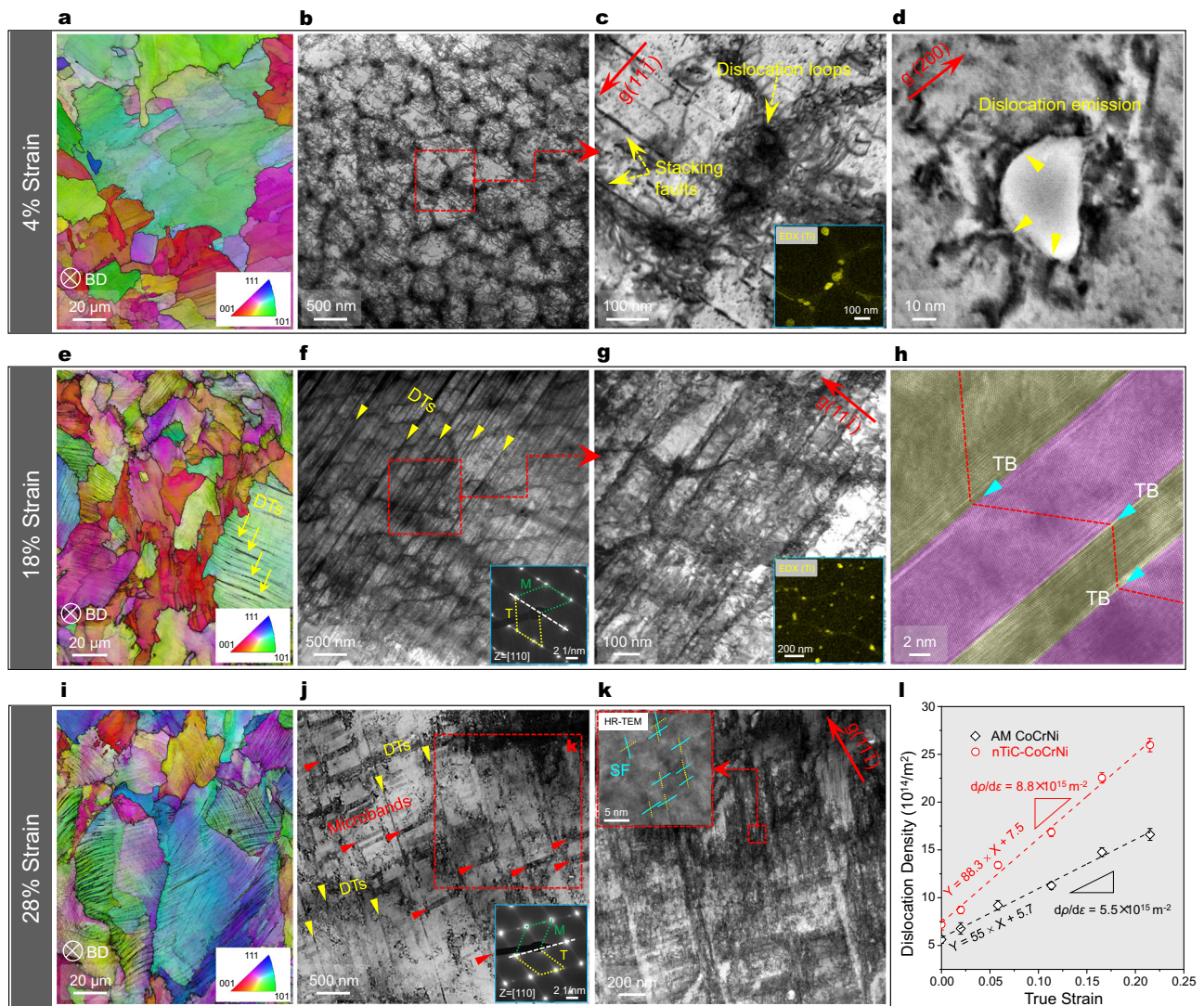


**Fig. 4 | Representative deformation substructure of the nTiC-CoCrNi alloy cryogenically (87 K) deformed to total tensile strains of 4%, 18% and 28%, respectively.** **a** EBSD IPF plus image quality (IQ) map showing the absence of deformation twins (DTs) at 4% strain. **b, c** BF-STEM images showing dislocation loops around TiC nanoprecipitates. The EDX Ti mapping is shown as inset in (**a**) to indicate the position of TiC precipitates. **d** BF-STEM image exhibiting dislocation emission from the TiC-matrix interface. **e** EBSD IPF plus IQ map, **f, g** BF-STEM and selected-area electron diffraction (SAED) images, and **h** HR-TEM image showing the formation of DTs at 18% strain. A markedly higher dislocation density within

cellular structures is observed in the nTiC-CoCrNi alloy when comparing (**g**) and Supplementary Fig. 13 (the AM CoCrNi sample) taken under the same  $g = 11\bar{1}$  diffraction vector. **i** EBSD IPF plus IQ map, **j, k** BF-STEM images along with the SAED image showing the formation of more DTs as well as their interaction with dislocation microbands. A HR-TEM image showing the presence of high number density stacking faults (SFs) is inset in (**k**). **l** The evolution of the overall dislocation density as a function of true strain (measured from neutron diffraction data), in comparison to the precipitate-free AM CoCrNi reference sample. The error bars represent standard deviation. Source data are provided as a Source Data file.

plastic deformation prior to fracture). Instead, the fracture of this sample at the cryogenic temperature is driven by a ductile mode of microvoid nucleation, growth and coalescence (Fig. 5e and f). Given that the presence of TiC nanoprecipitates only marginally influences the grain boundary chemistry and thus the intrinsic cohesion, the suppression of intergranular cracks of the nTiC-CoCrNi alloy can be assumed to come from the mitigated interaction between lattice defects (dislocations and twins) and GBs. On one hand, the high number density of the TiC nanoprecipitates essentially increases the dislocation bow-out stress<sup>41</sup>, thereby enhancing the critical resolved shear stress (CRSS) for the generation of stacking fault loops and thus for the growth of deformation twins based on the double-cross-slip mechanism (see more detailed CRSS calculations in Supplementary Note 4)<sup>42–44</sup>. The increased stacking fault energy due to the increased concentration of C and Ti in solid solution also suppresses the formation of deformation twinning in the nTiC-CoCrNi

sample (Supplementary Figs. 15 and 16). On the other hand, the impenetrable TiC nanoprecipitates frequently block the growth of deformation twins (Fig. 5h and i) as well as the motion of dislocations, thus homogenizing defect distribution. This reduces the likelihood that these defects can accumulate excessively at GBs<sup>45</sup>.

It should be noted that the characteristics of the TiC-associated hetero-interfaces and the particle size are crucial for embrittlement under cryogenic conditions. Particularly when these particles become incoherent to the matrix, e.g., in the  $\mu$ TiC-CoCrNi sample, the resulting increased interfacial energy is likely to induce brittle cracking along the TiC-matrix interfaces, as shown in Fig. 5j–l. This explains the premature failure and the reduced ductility (~23.1%) observed in the  $\mu$ TiC-CoCrNi sample (Fig. 3a). This comparison further highlights the significance of introducing strong (non-shearable), nanosized and coherent precipitates for navigating the interplay between defect blocking (lending strength) and damage tolerance (lending ductility

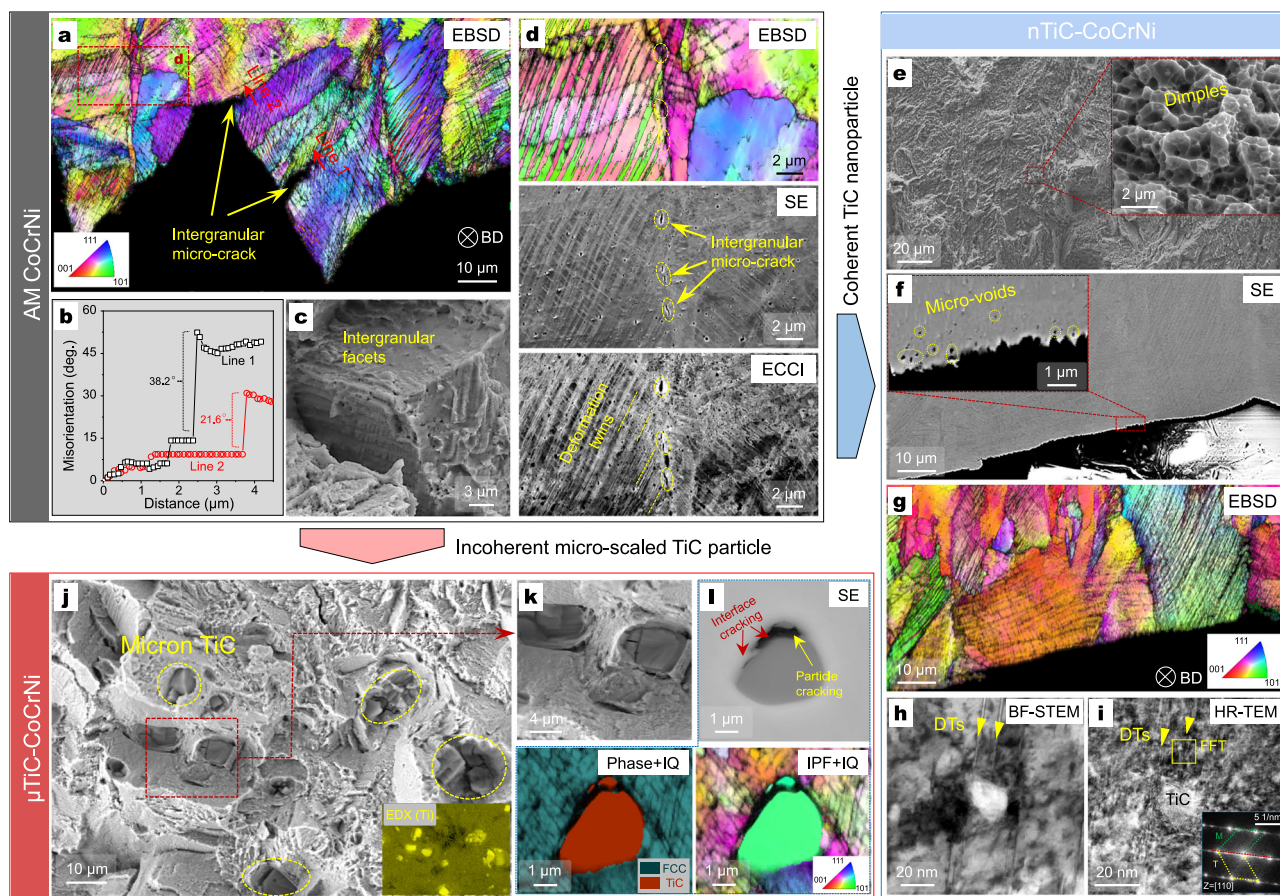


**Fig. 5 | Fracture and damage micromechanisms of AM CoCrNi, nTiC-CoCrNi and  $\mu$ TiC-CoCrNi samples deformed at 87 K. a** EBSD IPF plus IQ map of the fracture surface region of the AM CoCrNi sample, showing intergranular cracking. **b** The misorientation distribution across the two intergranular cracks marked in (a). **c** The fracture morphology of the AM CoCrNi, showing distinct intergranular facets. **d** EBSD IPF plus IQ map, SE and ECCI images of a magnified grain boundary region, showing the formation of micro-sized cracks or voids at the twin-grain boundary interactions. **e** The fracture morphology of the nTiC-CoCrNi sample, showing a ductile dimple-typed fracture behavior. **f** SE and **g** EBSD IPF plus IQ map probed close to the fracture surface, showing the absence of intergranular cracking and

the presence of high number-density microvoids. **h** BF-STEM and **i** HR-TEM images of the nTiC-CoCrNi sample cryogenically deformed to 18% strain, showing the blocking effect of TiC nanoprecipitate on the growth of deformation twins. **j, k** The fracture morphology of the  $\mu$ TiC-CoCrNi sample, showing a locally brittle fracture behavior of particle fracture and interface debonding. The inserted EDX Ti mapping in (j) marks the position of unmelted TiC particles. **l** The SE image and EBSD results taken close to the fracture surface of the  $\mu$ TiC-CoCrNi sample, validating the occurrence of interface debonding between the matrix and the micro-sized TiC particles as well as the particle cracking. Source data are provided as a Source Data file.

and fracture toughness) in the field of AM alloys at cryogenic temperatures.

We note here that our method of introducing TiC nanoprecipitates is significantly different from that achieved by pre-alloying and associated precipitation during cyclic reheating, in terms of the dissolution and subsequent precipitating kinetics and the resulting types of precipitates. In order to study the difference in more detail, we prepared pre-alloyed powders which were additionally microalloyed with nearly the same amount of C and Ti as in our nTiC-CoCrNi sample (Supplementary Table 3). After the L-PBF process of this sample (referred to as CoCrNi(TiC)), in addition to TiC nanoprecipitates, we also observe a usually unavoidable formation of Cr-rich  $M_{23}C_6$  precipitates at GBs (Supplementary Fig. 17), which induces severe intergranular cracking during cryogenic deformation, thus deteriorating ductility to only -27.2% (Supplementary Fig. 18). These findings suggest that during the L-PBF process of the nTiC-CoCrNi sample, the reprecipitation of TiC is highly preferential over other types of precipitates. We attribute this phenomenon to the heterogeneously distributed Ti and C solutes, or more specifically local modulation of Ti and C clusters, likely developed after the instantaneous laser melting of TiC and the subsequent rapid solidification. This preferential reprecipitation

process further implies that our nanoparticle strategy is not limited to specific alloy systems. In addition to the CoCrNi alloy that has been selected here as a model matrix material for demonstrating our approach, we show that TiC nanoparticles with similar characteristics can also be introduced in other additively manufactured FCC materials, including austenitic stainless steels and  $Fe_{60}Co_{15}Cr_{15}Ni_{10}$  (in at.%) MEA, using the same processing method to enhance their cryogenic strength-ductility combination (Supplementary Figs. 19 and 20).

To conclude, we presented here a novel additive manufacturing pathway that effectively enhanced the cryogenic strength and ductility of AM FCC alloys through in-situ formation of hard and stiff second-phase particles, which are typically challenging to metallurgically control during additive manufacturing processes due to their high melting points. We showed that through the laser-induced melting of size-controlled pre-assembled TiC particles and their kinetically favorable reprecipitation during additive manufacturing, an unprecedented high number-density ( $\sim 4.9 \times 10^{20} m^{-3}$ ) of coherent, nanosized TiC precipitates ( $\sim 36$  nm) can be introduced within the microstructure of a CoCrNi alloy. The fine-tuning of these precipitates by this approach and their interactions with microstructural defects (e.g., dislocations and twins) upon mechanical loading triggered an

exceptionally high product of strength and ductility of 60.8 GPa % at near liquid-nitrogen temperature, surpassing all other AM alloys at the same yield strength level (~1 GPa) documented to date. Unlike other in-situ microstructure tuning approaches that explored alloy-specific phase transformations during laser-induced cyclic reheating<sup>15,16</sup>, we demonstrated that our method of introducing well-controlled nanoparticles can generally be extended to other FCC materials (like austenite stainless steels) for better cryogenic mechanical performance. Our work thus provides a general pathway to advance the use of AM alloys in extreme cryogenic environments.

## Methods

### Alloy fabrication

In this investigation, pre-alloyed equiatomic powders of CrCoNi medium-entropy alloy (MEA), with a particle size distribution ranging from 15 to 53  $\mu\text{m}$ , were employed. In the case of nTiC-CoCrNi powders, TiC nanoparticles with a mean size of ~190 nm, were blended with CoCrNi powders to produce composite powders through the utilization of a planetary ball mill apparatus (Fritsch GmbH, Germany). In order to avoid the formation of coarse primary TiC precipitates, the fraction of TiC nanoparticles is experimentally optimized to 1.5 wt.%. The ball milling process was carried out under the following parameters: a ball-to-powder weight ratio of 2:1, a main disc rotation speed of 200 rpm, and a milling duration of 4 hours. In order to investigate the influence of the size of assembled TiC particles, larger TiC particles with an average size of 10  $\mu\text{m}$  (1.5 wt.%) were used to prepare the  $\mu\text{TiC-CoCrNi}$  powders, with the same blending procedure as that for nTiC-CoCrNi. Pre-alloyed CoCrNi(TiC) powders (nominal composition  $\text{Co}_{34.2}\text{Cr}_{30.2}\text{Ni}_{34.1}\text{Ti}_{1.2}\text{C}_{0.3}$ , in wt.%) with the same amount of C and Ti as that in nTiC-CoCrNi were produced by vacuum induction melting, followed by vacuum inert gas atomization and powder sieving, which yields a similar particle size as that of CrCoNi powders.

Additive manufacturing using the above four types of powders was conducted using an HBD-200 L-PBF system (Hanbang United 3D Tech Co., Ltd, China). Prior to L-PBF fabrication, alloy powders were sieved and then dried at 373 K in a vacuum chamber. Following extensive optimization of process parameters using an energy density approach<sup>46</sup>, the laser power, laser scanning speed, layer thickness, and hatching space were set as 175 W, 900 mm/s, 30  $\mu\text{m}$ , and 70  $\mu\text{m}$ , respectively. A scanning strategy involving a 67° rotation between adjacent layers was implemented to mitigate anisotropy in the transverse direction as well as to alleviate residual stresses in the as-printed materials, shown in Supplementary Fig. 1. The dimension of as-printed block specimens was 40 mm×12 mm×40 mm. All the AM samples exhibit a high density exceeding 99.5%. In order to investigate the effects of L-PBF processing parameters on reprecipitation behavior of TiC, a power from 125 W to 200 W and scanning rate from 600 mm/s to 1500 mm/s were selected, which yielded different volume energy density (VED) ranging from 40 J/mm<sup>3</sup> to 158 J/mm<sup>3</sup>, the microstructure and density shown in Supplementary Fig. 21 and Supplementary Table 4. In addition to block specimens, in order to reveal the nano-precipitation mechanism, single-track thin walls (a length of 10 mm) with a layer and ten layers on a 316 L substrate were prepared with the same L-PBF processing parameters with the block specimens. The measured chemical composition of the as-printed samples is listed in Supplementary Table 3.

### Mechanical testing

Dog-bone-like tensile specimens, with a gauge length of 10 mm and a width of 2.6 mm were machined along different planes from the as-printed samples. Quasi-static uniaxial tensile tests with a nominal engineering strain rate of  $1 \times 10^{-3} \text{ s}^{-1}$  were performed inside an environment chamber at the room (298 K) and cryogenic temperature (87 K). The strain was measured by a mechanical extensometer with a gauge length of 10 mm (epsilon LHT). At least five tensile specimens for each

condition were tested to ensure the repeatability. Interrupted tensile tests at different engineering strains (4%, 18% and 28%) of the nTiC-CoCrNi and AM CoCrNi samples were conducted with the aim to study the deformation behavior. Compact-tension (C(T)) specimens for the measurement of fracture toughness were machined from the as-printed blocks. According to the ASTM standard E1820<sup>47</sup>, C(T) specimens with a width ( $W$ ) of 25 mm, a thickness ( $B$ ) of 9 mm and a notch length of ~13 mm were prepared by electrical discharge machining (EDM). Fatigue pre-cracking was introduced at the ambient temperature at a stress intensity range ( $\Delta K$ ) of ~15 MPa·m<sup>0.5</sup>, a frequency of 10 Hz and a load ratio of 0.1. Optical microscopy was used to examine the length of the fatigue crack from both sides of the specimens, to ensure the linearity of the crack front. The final length of the fatigue crack was around 14.5 mm, well above the minimum length (~1.3 mm) regulated by ASTM E1820<sup>47</sup>. More details of fracture toughness testing and the associated calculation can be found in Supplementary Note 5 and Supplementary Fig. 9. At least three fracture toughness specimens were tested to ensure the repeatability.

### Microstructural characterization

The scanning electron microscopy (SEM) observation was conducted using a ZEISS Gemini 2 instrument equipped with SE, ECCI, and EBSD detectors. The acquired EBSD data were analyzed using the TSL OIM software package. To study the interface relationship between TiC nanoprecipitates and the matrix, TEM characterization was performed by an aberration-corrected transmission electron microscope (FEI Titan G2 60–300) under 300 kV. The dislocation patterning in non-deformed and deformed samples was studied using a FEI Talos F200X TEM operated at an accelerating voltage of 200 kV. The elemental distribution was detected using EDX. Thin foils for TEM observations were prepared by either focused ion beam (FIB), using a Zeiss-Cross Beam XB 1540 FIB-SEM instrument or electro-polished (electrolyte of 20 vol.% perchloric acid and 80 vol.% acetic acid, at 258 K and 50 mA). The weak-beam TEM dark-field imaging was conducted to accurately determine the dislocation patterns at different strains using a diffraction vector of  $\mathbf{g} = 11\bar{1}$ . The number density of TiC nanoprecipitates per unit area was measured based on the TEM-based EDX mapping, and it was then converted to the value per unit volume considering the FIB sample thickness using the relation established in ref. 48. FFT images obtained from the TEM images were calculated using the Gatan Digital Micrograph 3.5 software.

APT measurement was conducted using an instrument of local electrode atom probe LEAP 5000XR (Cameca Instrument Inc.). Experiments were operated in the high-voltage laser pulsing mode with a laser pulse energy of 45 pJ and a base temperature of 60 K. A detection rate of 5 ions detected for 1000 pulses and a laser pulse repetition rate 200 kHz were used for data collection. Needle-shaped APT specimens were fabricated using a FEI Helios NanoLab 600i dual beam SEM/FIB with Ga source. The data analysis and reconstruction were performed using the commercial software package AP Suite 6.1. The characterization of the distribution of manufacturing defects was carried out through  $\mu\text{-CT}$  technique using a GE phoenix Nanotom device operated at 140 kV, 100  $\mu\text{A}$ , and 1500 ms detector timing. The radiographic images, obtained at a spatial resolution of 0.8  $\mu\text{m}$ , were reconstructed using the VG Studio Max 2.2 software. Neutron diffraction experiments were conducted at the China Spallation Neutron Source (CSNS) using a Multi-Physics Instrument equipped with a 360° rotation stage. The neutron source was operated at a power of 120 kW, and data collection was performed using the time-of-flight method, with a total scanning time of 1 hour. The specimens were rotated at a rate of 6°/min perpendicular to the incident neutron beam direction to mitigate the impact of textures. The evolution of dislocation density in AM CoCrNi and nTiC-CoCrNi samples under various interrupted strains (0%, 2%, 6%, 12%, 18%, and 25%) was determined using the modified Williamson-Hall (MWH)<sup>49</sup> and Warren-Averbach (MWA)<sup>50</sup>

methods, utilizing neutron diffraction profiles as depicted in Supplementary Fig. 22. The exact Bragg position and the full width at half maximum (FWHM) were determined by Rietveld refinement performed using the GSAS-II software. Additional details regarding the calculation methodology can be found in Supplementary Note 6.

### Thermodynamic and thermal-history simulations

A 3D computational fluid dynamics (CFD) model was created to simulate the transient processes of melting and solidification of the powder particles<sup>51</sup>. The governing equations, boundary conditions, and source terms, etc. related to CFD simulations were provided in Supplementary Note 7. The powder layer was generated by modeling a rake being pushed over a powder bed using the discrete element method (DEM). The distribution information of powder bed particles obtained during powder laying was imported into the CFD model, and the thermal history of the printing process was solved using discrete metal powder particles as objects. After each layer of powder bed was melted and solidified, the morphological features (including the fusion zone and un-melted powders) were saved in STL file format and imported into the DEM model as the substrate for the new layer. It was assumed that the first printed layer could be sufficiently cooled to room temperature before the laser power input for the second layer<sup>52</sup>. The powders were then spread to form a new layer of powder bed, and repeat the above process to complete the simulation of multi-layer powder bed printing. The process parameters used for the simulation were consistent with those of the L-PBF experiment. Due to the absence of some physical parameters of CoCrNi powders, the 316 L powders were selected as the base powders to perform the thermal-history simulation.

The equilibrium phase fractions as a function of temperature were calculated using the Thermo-Calc software 2024a together with the TCHEA4 thermodynamic database for high entropy alloys. Particle dissolution simulations were performed using the DICTRA module of the Thermo-Calc software in conjunction with the TCHEA7 thermodynamic database and the MOBHEA3 mobility database for high-entropy alloys<sup>53</sup>. More details about DICTRA simulations were described in Supplementary Note 8.

### Data availability

The data generated in this study have been deposited in the public community repository Figshare: <https://doi.org/10.6084/m9.figshare.30567389><sup>54</sup>. Source data are provided with this paper and in the Supplementary Information file. Source data are provided with this paper.

### References

- Gu, D. et al. Material-structure-performance integrated laser-metal additive manufacturing. *Science* **372**, 1487 (2021).
- Raabe, D., Tasan, C. C. & Olivetti, E. A. Strategies for improving the sustainability of structural metals. *Nature* **575**, 64–74 (2019).
- Liu, L. et al. Dislocation network in additive manufactured steel breaks strength-ductility trade-off. *Mater. Today* **21**, 354–361 (2018).
- Wang, Y. et al. Additively manufactured hierarchical stainless steels with high strength and ductility. *Nat. Mater.* **17**, 63–71 (2018).
- Tan, C. et al. Progress and perspectives in laser additive manufacturing of key aeroengine materials. *Int. J. Mach. Tool. Man.* **170**, 103804 (2021).
- Mukherjee, T. et al. Control of grain structure, phases, and defects in additive manufacturing of high-performance metallic components. *Prog. Mater. Sci.* **138**, 101153 (2023).
- Weng, F. et al. Influence of oxides on the cryogenic tensile properties of the laser aided additive manufactured CoCrNi medium entropy alloy. *Compos. Part B-Eng.* **216**, 108837 (2021).
- Kumar, P. et al. On the strength and fracture toughness of an additive manufactured CrCoNi medium-entropy alloy. *Acta Mater.* **258**, 119249 (2023).
- Kim, Y., Kim, M. & Lee, K. 1.45 GPa ultrastrong cryogenic strength with superior impact toughness in the in-situ nano oxide reinforced CrMnFeCoNi high-entropy alloy matrix nanocomposite manufactured by laser powder bed fusion. *J. Mater. Sci. Technol.* **97**, 10–19 (2022).
- Gludovatz, B. et al. Exceptional damage-tolerance of a medium-entropy alloy CrCoNi at cryogenic temperatures. *Nat. Commun.* **7**, 10602 (2016).
- Liu, D. et al. Exceptional fracture toughness of CrCoNi-based medium- and high-entropy alloys at 20 kelvin. *Science* **378**, 978–983 (2022).
- Wang, F. Mechanical property study on rapid additive layer manufacture Hastelloy® X alloy by selective laser melting technology[J]. *Inter. J. Adv. Manuf. Tech.* **58**, 545–551 (2012).
- Mostafaei, A. et al. Additive manufacturing of nickel-based superalloys: A state-of-the-art review on process-structure-defect-property relationship. *Prog. Mater. Sci.* **136**, 101108 (2023).
- Peng, H. et al. Microstructure, mechanical properties and cracking behaviour in a  $\gamma'$ -precipitation strengthened nickel-base superalloy fabricated by electron beam melting. *Mater. Des.* **159**, 155–169 (2018).
- Kürnstener, P. et al. High-strength Damascus steel by additive manufacturing. *Nature* **582**, 515–519 (2020).
- Tan, C. et al. Machine Learning Customized Novel Material for Energy-Efficient 4D Printing. *Adv. Sci.* **10**, 2206607 (2023).
- Sames, W. et al. The metallurgy and processing science of metal additive manufacturing. *Inter. Mater. Rev.* **61**, 315–360 (2016).
- Zhang, J. et al. Ultrauniform, strong, and ductile 3D-printed titanium alloy through bifunctional alloy design. *Science* **383**, 639–645 (2024).
- Liu, Y. et al. Manufacturing of high strength and high conductivity copper with laser powder bed fusion. *Nat. Commun.* **15**, 1283 (2024).
- Qu, M. et al. Melting and solidification dynamics during laser melting of reaction-based metal matrix composites uncovered by in-situ synchrotron X-ray diffraction. *Acta Mater.* **271**, 119875 (2024).
- Ardell, A. Precipitation Hardening. *Metall. Trans. A* **16A**, 1985–2131 (1985).
- Fernie, J., Drew, R. & Knowles, K. Joining of engineering ceramics. *Inter. Mater. Rev.* **54**, 283–331 (2013).
- Fine, M., Brown, L. & Marcus, H. Elastic constants versus melting temperature in metals. *Scr. Metall.* **18**, 951–956 (1984).
- Amar, A. et al. Additive manufacturing of VCoNi medium-entropy alloy: Microstructure evolution and mechanical properties. *Addit. Manuf.* **68**, 103522 (2023).
- Poza, P. & Llorca, J. Fracture toughness and fracture mechanisms of Al-Al<sub>2</sub>O<sub>3</sub> composites at cryogenic and elevated temperatures. *Mater. Sci. Eng. A* **206**, 183–193 (1996).
- Kuramoto, S., Itoh, G. & Kanno, M. Intergranular Fracture in Some Precipitation-Hardened Aluminum Alloys at Low Temperatures. *J. Metall. Mater. Trans. A* **27**, 3081–3088 (1996).
- Xiang, M. et al. Facile synthesis of high-melting point spherical TiC and TiN powders at low temperature. *J. Am. Ceram. Soc.* **103**, 889–898 (2020).
- Bertsch, K. et al. Origin of dislocation structures in an additively manufactured austenitic stainless steel 316. L. *Acta Mater.* **199**, 19–33 (2020).
- Frage, N., Froumin, N. & Dariel, M. Wetting of TiC by non-reactive liquid metals. *Acta Mater.* **50**, 237–245 (2002).
- Ritchie, R. O. The conflicts between strength and toughness. *Nat. Mater.* **10**, 817–822 (2011).
- Han, L. et al. A mechanically strong and ductile soft magnet with extremely low coercivity. *Nature* **608**, 310–316 (2022).
- Han, L. et al. Ultrastrong and Ductile Soft Magnetic High-Entropy Alloys via Coherent Ordered Nanoprecipitates. *Adv. Mater.* **33**, 2102139 (2021).

33. Kim, S. et al. Strain hardening recovery mediated by coherent precipitates in lightweight steel. *Sci. Rep.* **11**, 14468 (2021).
34. Yao, M. et al. Strengthening and strain hardening mechanisms in a precipitation-hardened high-Mn lightweight steel. *Acta Mater.* **140**, 258–273 (2017).
35. Xu, H. et al. The synchronous improvement of strength and plasticity (SISP) in new Ni-Co based disc superalloys by controlling stacking fault energy. *Sci. Rep.* **7**, 8046 (2017).
36. Dodd, S. P., Cankurtaran, M. & James, B. Ultrasonic determination of the elastic and nonlinear acoustic properties of transition-metal carbide ceramics: TiC and TaC. *J. Mater. Sci.* **38**, 1107–1115 (2003).
37. Geng, W., Freeman, A. & Olson, G. Influence of alloying additions on grain boundary cohesion of transition metals: First-principles determination and its phenomenological extension. *Phys. Rev. B* **63**, 165415 (2001).
38. Ming, K. et al. Grain boundary decohesion by nanoclustering Ni and Cr separately in CrMnFeCoNi high-entropy alloys. *Sci. Adv.* **5**, 639 (2019).
39. Schweinfest, R., Paxton, A. & Finnis, M. Bismuth embrittlement of copper is an atomic size effect. *Nature* **432**, 1008–1011 (2004).
40. Zhang, Y. et al. Deformation-twin-induced grain boundary failure. *Scr. Mater.* **66**, 117–120 (2012).
41. Bacon, D., Kocks, U. & Scattergood, R. The effect of dislocation self-interaction on the orowan stress. *Philos. Mag.* **28**, 1241–1263 (1973).
42. Zhao, Y. et al. Heterogeneous precipitation behavior and stacking-fault-mediated deformation in a CoCrNi-based medium-entropy alloy. *Acta Mater.* **138**, 72–82 (2017).
43. Chen, M. et al. Deformation Twinning in Nanocrystalline Aluminum. *Science* **300**, 1275–1277 (2003).
44. Lagerlöf, K., Castaing, J., Pirouz, P. & Heuer, A. Nucleation and growth of deformation twins: A perspective based on the double cross-slip mechanism of deformation twinning. *Philos. Mag.* **90**, 2841–2854 (2002).
45. Cheng, H. et al. The influence of L<sub>12</sub> ordered precipitates on hydrogen embrittlement behavior in CoCrNi-based medium entropy alloys. *Acta Mater.* **260**, 119328 (2023).
46. Prashanth, K. et al. Is the energy density a reliable parameter for materials synthesis by selective laser melting? *Mater. Res. Lett.* **5**, 386–390 (2017).
47. E08 Committee, E1820-13 Standard Test Method for Measurement of Fracture Toughness (ASTM International, 2013).
48. Zhang, R. et al. Direct imaging of short-range order and its impact on deformation in Ti-6Al. *Sci. Adv.* **5**, x2799 (2019).
49. Ungár, T., Révész, Á & Borbély, A. Dislocations and grain size in electrodeposited nanocrystalline Ni determined by the Modified Williamson-Hall and Warren-Averbach procedures. *J. Appl. Crystallogr.* **31**, 554–558 (1998).
50. Ungár, T. et al. Dislocations, grain size and planar faults in nanostructured copper determined by high resolution X-ray diffraction and a new procedure of peak profile analysis. *Acta Mater.* **10**, 3693–3699 (1998).
51. Yang, M., Wang, L. & Yan, W. Phase-field modeling of grain evolutions in additive manufacturing from nucleation, growth, to coarsening. *NPJ Comput. Mater.* **7**, 1–12 (2021).
52. Ren, N. et al. Solute trapping and non-equilibrium microstructure during rapid solidification of additive manufacturing. *Nat. Commun.* **14**, 7990 (2023).
53. J.-O. Andersson, Helander, T., Höglund, L., Shi, P. & Sundman, B. Thermo-Calc & DICTRA, computational tools for materials science. *Calphad* **26**, 273–312 (2002).
54. T. Lu, et al. Supporting data for: In-situ nano-precipitation enables superior cryogenic mechanical properties in a 3D printable medium-entropy alloy. figshare <https://doi.org/10.6084/m9.figshare.30567389> (2025).
55. Han, B. et al. Additively manufactured high strength and ductility CrCoNi medium entropy alloy with hierarchical microstructure. *Mater. Sci. Eng. A* **820**, 141545 (2021).
56. Lu, T. et al. Exceptional strength-ductility combination of additively manufactured high-entropy alloy matrix composites reinforced with TiC nanoparticles at room and cryogenic temperatures. *Addit. Manuf.* **56**, 102918 (2022).
57. Kumar, P. et al. A strong fracture-resistant high-entropy alloy with nano-bridged honeycomb microstructure intrinsically toughened by 3D-printing. *Nat. Commun.* **15**, 841 (2024).
58. Li, J. et al. Phase transformation - induced strengthening of an additively manufactured multi- principal element CrMnFeCoNi alloy. *Mater. Des.* **195**, 108999 (2020).
59. Smith, C. T. et al. A 3D printable alloy designed for extreme environments. *Nature* **617**, 513–518 (2023).
60. Tran, M. et al. Effect of hot isostatic pressing on the cryogenic mechanical properties of CrCoNi medium entropy alloy processed by direct energy deposition. *Mater. Sci. Eng. A* **828**, 142110 (2021).
61. Karthik, G. et al. Delayed deformation-induced martensite transformation and enhanced cryogenic tensile properties in laser additive manufactured 316L austenitic stainless steel. *Addit. Manuf.* **47**, 102314 (2021).
62. Tang, L. et al. Mechanical performance and deformation mechanisms at cryogenic temperatures of 316L stainless steel processed by laser powder bed fusion: In situ neutron diffraction. *Scr. Mater.* **218**, 114806 (2022).
63. Park, J., Kim, B. & Kim, J. Mechanical Properties of Laser-Powder Bed Fusion Processed Fe-15Cr-6Ni-6Mn Multi-phase Steel at Room and Cryogenic Temperatures. *Met. Mater. Inter.* **29**, 3521–3531 (2023).
64. Mishra, P. et al. Microstructural characterization and mechanical properties of additively manufactured 21-6-9 stainless steel for aerospace applications. *J. Mater. Res. Technol.* **25**, 1483 (2023).
65. Poudel, A. et al. Tensile deformation behavior of laser powder direct energy deposited Inconel 625: Cryogenic to elevated temperatures. *Mater. Sci. Eng. A* **889**, 145826 (2024).
66. Ahmad, N. et al. Revealing deformation mechanisms in additively manufactured Alloy 718: Cryogenic to elevated temperatures. *Mater. Sci. Eng. A* **849**, 143528 (2022).
67. Zang, M. et al. Achieving highly promising strength-ductility synergy of powder bed fusion additively manufactured titanium alloy components at ultra-low temperatures. *Addit. Manuf.* **65**, 103444 (2023).

## Acknowledgements

X.-C.Z. acknowledges the financial support from the National Key Research and Development Program (2022YFB4602100). T.L. is sponsored by the National Natural Science Foundation of China (No. 52575177, No. 52205152), Shanghai Pujiang Programme (No. 23FJD023), and Shanghai Gaofeng Project for University Academic Program Development. B.S. acknowledges the financial support from the National Key R&D Program of China (No. 2023YFB3712100) and the National Natural Science Foundation of China (Grant No. 52275147). Z.S. acknowledges financial support from the Young Individual Research Grant (No. M22K3c0096) from the Agency for Science, Technology and Research of Singapore.

## Author contributions

T.L. and B.S. designed the research. T.L. and X.C. fabricated the medium-entropy alloy materials. T.L., X.C., and H.C. performed the mechanical tests. T.L. and N.Y. conducted the SEM and EBSD characterizations. X.D. and B.S. conducted the APT measurement. T.L. and B.W. conducted the neutron diffraction characterization and analysis. X.C. and J.T.

conducted the fracture toughness tests and analysis. B.S. performed the thermodynamic calculation. T.L. and Y.C. carried out the TEM characterization. X.Y. carried out the molecular dynamics calculation. A.K.S. and H.L. conducted thermal-history and DICTRA simulations. T.L., B.S., and D.R. analyzed the data and wrote the manuscript. B.S., D.R., S.S., Z.S., and X.-C.Z. revised the manuscript. X.-C.Z., D.R., and S.-T.T. supervised the study. All the authors discussed the results and commented on the manuscript.

### Competing interests

The authors declare no competing interests.

### Additional information

**Supplementary information** The online version contains supplementary material available at <https://doi.org/10.1038/s41467-025-67279-2>.

**Correspondence** and requests for materials should be addressed to Binhan Sun, Xian-Cheng Zhang or Dierk Raabe.

**Peer review information** *Nature Communications* thanks Peeyush Nandwana and the other anonymous reviewer(s) for their contribution to the peer review of this work. A peer review file is available.

**Reprints and permissions information** is available at <http://www.nature.com/reprints>

**Publisher's note** Springer Nature remains neutral with regard to jurisdictional claims in published maps and institutional affiliations.

**Open Access** This article is licensed under a Creative Commons Attribution-NonCommercial-NoDerivatives 4.0 International License, which permits any non-commercial use, sharing, distribution and reproduction in any medium or format, as long as you give appropriate credit to the original author(s) and the source, provide a link to the Creative Commons licence, and indicate if you modified the licensed material. You do not have permission under this licence to share adapted material derived from this article or parts of it. The images or other third party material in this article are included in the article's Creative Commons licence, unless indicated otherwise in a credit line to the material. If material is not included in the article's Creative Commons licence and your intended use is not permitted by statutory regulation or exceeds the permitted use, you will need to obtain permission directly from the copyright holder. To view a copy of this licence, visit <http://creativecommons.org/licenses/by-nc-nd/4.0/>.

© The Author(s) 2025